"Gold Nanoprism-Nanorod Face Off: Comparing the heating efficiency, cellular internalisation and thermoablation capacity of gold nanorods and nanoprisms"

Gabriel Alfranca Ramón[1,2§], Álvaro Artiga[1§], Grazyna Stepien[3], María Moros[4], Daxiang Cui[2], Scott G. Mitchell[1*] and Jesús M. de la Fuente[1,2,*]

1 –Instituto de Ciencia de Materiales de Aragón (ICMA-CSIC), Universidad de Zaragoza, 50009-Zaragoza, Spain;

2 – Institute of Nano Biomedicine and Engineering, Key Laboratory for Thin Film and Microfabrication Technology of the Ministry of Education, Shanghai Jiao Tong University, 200240-Shanghai, P. R. China;

3 – Instituto de Nanociencia de Aragón, Universidad de Zaragoza, 50018-Zaragoza, Spain;

4 - Istituto di Scienze Applicate e Sistemi Intelligenti "Eduardo Caianiello", 80078-Naples, Italy.

Authors for correspondence: *scott@unizar.es, *jmfuente@unizar.es

§ these authors contributed equally to this publication

Abstract

Aim: To compare the synthesis, heating capability, extent of cellular internalisation and thermoablation capacity of two types of anisotropic gold nanoparticles (AuNPs): gold nanorods (NRs) and nanoprisms (NPrs). Methods: Gold nanoprisms (NPrs) and nanorods (NRs) with surface plasmon resonance (SPR) absorption bands in the near-infra-red (NIR) range were synthesised and their heating efficiency upon irradiation with a NIR-laser (1064 nm) was evaluated. Their cellular internalisation, location and toxicity were then assessed in the Vero cell line by TEM and ICP analysis and their ability to induce cell death upon laser irradiation was then assessed and compared. Results: poly(ethylene) glycol (PEG)-stabilised NPrs and NRs produced no cytotoxic effects and TEM studies showed that both types of nanoparticles are accumulated inside lysosomes, where NPrs displayed a far greater cellular internalisation. Although NRs possessed a more efficient heating capability during 10 min irradiation with a NIR laser, *in vitro* thermoablation studies clearly demonstrated that NPrs were more effective at inducing cell death. Conclusion: While both NRs and NPrs are each highly efficient heat mediators with the potential to induce cell death, the combined heating and cell internalisation properties of NPrs make them more appropriate for photothermal cell ablation studies.

Keywords (5-10 words): plasmonic gold nanoparticles, hyperthermia, photothermal cell ablation, Near Infra-Red, cellular internalisation

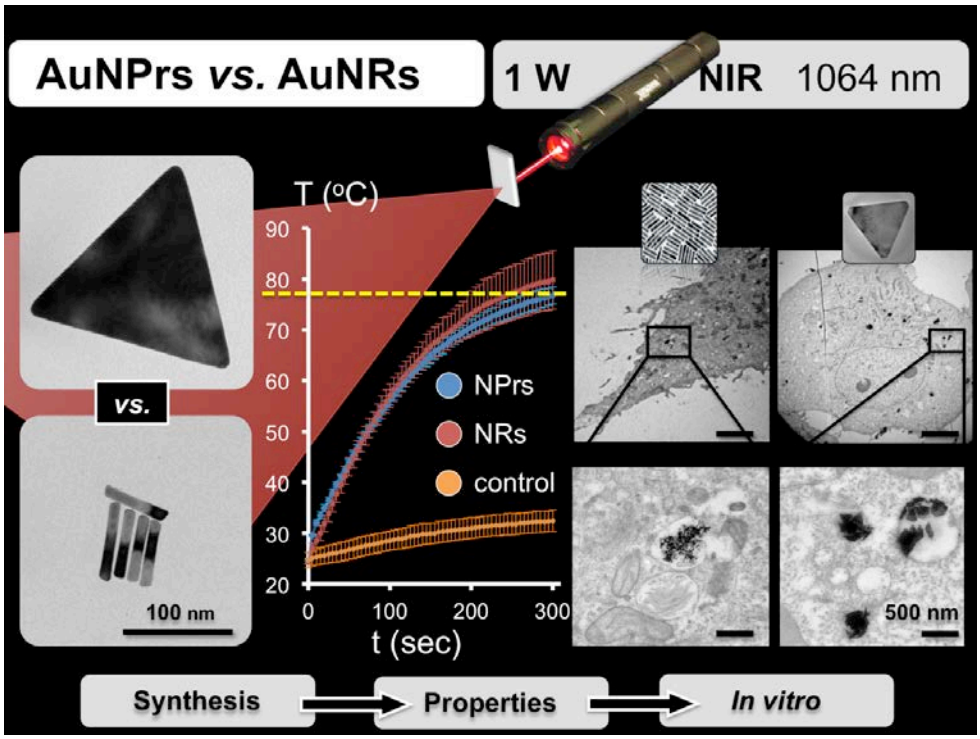

Table of Contents Graphic

1. Introduction

The ability of nanomaterials to convert light energy into heat, the photothermal effect, is a characteristic and versatile property applicable to many biomedical applications including photothermal therapy [1-3], drug delivery [4–6], optoacoustic imaging [7, 8] and biosensing [9], among others [10]. The photothermal treatment of solid tumours by thermoablation has reached the stage of clinical trials [11].

Nanoparticle (NP)-mediated photothermal therapy (PTT) is a promising cancer treatment consisting of the use of heat to kill tumour cells (thermoablation) or weaken them, thereby making them more susceptible to other treatment(s), where the latter translates into a synergistic therapeutic improvement [12] allowing for a reduction in the effective dose of other aggressive therapies currently applied such as radio and chemotherapies [13,14]. The local (cellular) destructive effect of increased temperature corresponds to damage of cellular structures, mainly lysosomes, releasing their content and inducing cell death [15]. The two major causes, or mechanisms, of the synergistic effect are that increased oxygenation prevents hypoxic resistance [12]; and also that increased heat promotes the expression of ligands on the surface of cancer cells that transmit *'eat me'* signals. These ligands act as cytokines and stress ligands, inducing dendritic cells and macrophages to produce pro-inflammatory cytokines thereby making tumour cells more susceptible to lysis by natural killer cells [16].

Nevertheless, delivering and controlling heat *in vivo* represents a significant challenge, primarily because to the best of our knowledge, many of the currently available devices are able to selectively destroy a deeply situated cancer without destroying the surrounding healthy tissues [12]. Fortunately, nanotechnology can offer a wide variety of NPs that can function as nanoheaters [17], for example superparamagnetic NPs [18,19] as well as various types of plasmonic NPs [12,14,19] that act as nanotransducers that can be activated remotely by radiation which does not (or minimally) interact with physiological tissue and fluids.

From the extensive range of inorganic plasmonic NPs for biomedical applications [20,21], the physicochemical properties of gold nanoparticles (AuNPs) have given them a singular ubiquity in the field

of nanomedicine [12,14,22]. Their unique optical properties [12], biocompatibility [23,24], and ease of surface modification [19,25] means that there has been intense and prolonged interest in AuNPs for bioapplications [26]. Furthermore, the size-dependent physicochemical properties can be modified with ease using simple synthetic protocols [27,28], meaning that AuNPs can be viewed as a highly accessible modular library of nanomaterials for use in nanomedicine.

The optical properties of nanomaterials are mainly governed by the surface plasmon effect that relates to coherent oscillations of conduction electrons on a metal surface excited by electromagnetic radiation at a metal–dielectric interface [28]. Further, the optical properties of metallic structures are shown to be influenced primarily by the surface plasmon resonance (SPR) of conduction electrons, the frequency of which is determined by the nature of the metal, but is also sensitive to refractive index changes around the metal in combination with various other parameters, including the surrounding medium. Localised surface plasmon resonances (LSPRs) are electromagnetic waves confined on metallic nanostructures [29]. The LSPR bands of pseudo-spherical AuNPs (with a diameter < 100 nm) lie in the visible region of the electromagnetic spectrum and the main contribution to the position of the LSPR band is the diameter of the NPs [30]. Thus, when high symmetry metal NPs are enlarged, their optical properties change only slightly, yet when anisotropy is added to the NP - such as growth of nanorods or nanoprisms -the optical properties of the nanoparticles change dramatically and are highly size-dependent [31]. As a result, for anisotropic NPs the major contribution to the UV−vis spectrum corresponds to the in-plane dipolar mode lying in the Near-Infrared (NIR) range [22]. Conveniently, the absorption profile of biological structures and living organisms is significantly lower in the so-called NIR *'biological window'*. Between *ca.* 750-1200 nm the absorption of biological systems is highly decreased, especially for cytochromes (e.g. hemoglobin) that lie in the visible region [31]. Consequently, across this wavelength range, radiation can penetrate deep into tissue without causing significant detrimental effect to biological structures [8,15]. The LSPR band of anisotropic AuNPs can be fine-tuned over a large wavelength in the NIR range, making them extremely relevant for applications in photothermal therapy [14,15].

Nevertheless, many of the methods to produce NIR-absorbing AuNPs rely on challenging syntheses with several complex steps and/or seed-mediated approaches involving the cationic surfactant cetyltrimethylammonium bromide (CTAB) [27,30]. This compound is said to be the most widely used and convenient surfactant for high-yielding syntheses of anisotropic particles such as gold nanorods (NRs) [30] and nanoprisms (NPrs) [22]. Both NRs and NPrs exhibit size-dependent optical properties and can be synthesised to exhibit strong absorption in the NIR range. Upon excitation by incident light, sharp local heating can be generated by the photothermal conversion of the absorbed light energy into local heating, rendering these particular anisotropic AuNPs as extremely efficient for NIR-induced heating [15,32]. One limiting factor is that the cationic surfactant CTAB is a well-known highly toxic component, and thus methods to exchange CTAB for other less cytotoxic surfactants or polymer coatings have been extensively reported [22,30,33]. The need for alternative methods to produce NIR-absorbing AuNPs without CTAB is of great importance, as recently highlighted by Murphy and co-workers, pioneering author of the seed-mediated approach involving CTAB [34]. Our group reported a high-yielding synthesis of NPrs which avoids the use of this surfactant and is subsequently stabilised with poly(ethylene) glycol (PEG) [22]. These particles have since been used for optoacoustic imaging [7,8], photothermal therapy [8,35] and in thermometric biosensing [9].

Although many manuscripts concerning the biotechnological applications of nanomaterials are published each day the direct comparison of the physicochemical properties of materials types is almost unheard of in the literature, with *in vitro* and *in vivo* comparisons even more rare [3]. This means that when it comes to comparing two types of materials, researchers are more often than not forced to draw conclusions from separate studies where they encounter dramatic variations in the nanoparticle size, types, surface coatings, LSPR band, specific photothermal excitation conditions, cell culture environments, and so on. Herein we provide a direct comparison between PEG-stabilised NPrs and NRs with near identical LSPR bands; focussing specifically on quantifying their individual heating capability, cellular internalisation and ability to induce cell death *in vitro* upon NIR-laser irradiation.

2. Materials & Methods

Hydrogen tetrachloroaurate (III) hydrate, sodium borohydride, sodium hydroxide, sodium thiosulfate ($Na_2S_2O_3$) and hexadecyltrimethylammonium bromide (CTAB) were purchased from Sigma-Aldrich and used as received. Potassium iodide (KI) and Silver nitrate ($AgNO_3$) were purchased from Panreac®. Hydroquinone was purchased from Alfa Aesar®. Complete Dulbeccos's modified Eagle's medium (DMEM™) and Phosphate Buffered Saline (PBS) and Dulbecco's Phosphate Buffered Saline (DPBS) supplemented with Ca^{2+} and Mg^{2+} were purchased from Lonza® (Basel, Switzerland). DMEM was supplemented with 10 % foetal bovine serum (FBS), 5 % glutamine and 5 % penicillin/streptomycin prior usage on any cell culture. Sephadex® columns were purchased from GE Healthcare. Prior to use, all glassware was washed with *aqua regia* and rinsed thoroughly with Milli-Q water from Millipore Q-POD® system. All nanoparticles suspensions were sterilised with 0.22 µm MilliPore® filters prior addition to cell cultures.

UV-Vis spectra were collected using a Cary 50 Probe® spectrophotometer from Varian. SEM images acquired using a field emission SEM Inspect F50 with an EDX system INCA PentaFETx3 (FEI Company, Eindhoven, The Netherlands) in an energy range between 0-30 keV. TEM images were collected using a FEI Tecnai T20 (FEI Europe, Eindhoven, Netherlands) working at 200 kV for nanoparticle characterization and at 80 kV for cell imaging. Nanoparticles were irradiated using a 3 W Laser Quantum Ventus laser (1064 nm) operating at a power output of 1100 mW, which illuminates the sample with a power per unit of area of *ca.* 3.3 W cm^{-2} at the sample position. Both bright-field, dark field and standard fluorescence images of the cells were obtained with a Nikon Eclipse Ti with FPS system equipped with a phase contrast system, dark field visualization system and 387±11/447±60 nm (DAPI) cube filter connected to NIS-Elements Microscope Imaging Software. The heat produced by the NPs under NIR-radiation was monitored using software developed by The University of Zaragoza using a Fiber Optic Temperature Sensor TPT-62 (Fiso Technologies Inc.). For the cell viability assays, MTT (3-(4,5-dimethylthiazol-2-yl)-2,5-diphenyltetrazolium bromide) was purchased from Invitrogen™ and the optical density at 555 nm was recorded using a plate reader (ELx800TM, Biotek (Thermo Scientific Multiskan GO UV/Vis microplate spectrophotometer)). For ICP elemental analysis, samples were evaluated by ICP-AES and/or ICP-MS using Optima 8300 (Perkin Elmer®).

2.1 Synthesis of triangular gold nanoprisms (NPrs)

NPrs with LSPR at *ca.* 1100 nm were prepared using a modification of a previously reported procedure [22] (Scheme 1a). Briefly, 60 µL 0.1 M KI solution was added to 220 mL 0.5 mM $Na_2S_2O_3$ (aq). 110 mL of this dilution (KI + $Na_2S_2O_3$) was added slowly to 200 mL 2 mM $HAuCl_4$ (aq) over a period of *ca.* 30 sec and aged for 4 min undisturbed. A second addition of 110 mL of KI + $Na_2S_2O_3$ was made and was once again allowed to stand for 4 min before one final addition of 70 mL $Na_2S_2O_3$. The final solution was kept undisturbed for 60 min. UV-vis spectra revealed a strong absorbance peak at >1000 nm as well as a minor absorption band at *ca*. 550 nm. Subsequent electron microscopy analysis revealed these to correspond to triangular gold nanoprisms (NPrs) and pseudospherical (polyhedral) gold nanoparticles, respectively. The concentration of NPrs was calculated using their LSPR peak absorbance at *ca.* 1100 nm and applying a conversion factor (ε) 29 mL mg^{-1} cm^{-1}. Note: ε was obtained from combined UV-vis spectroscopy/ICP analyses.

PEGylation of NPrs

NPrs were stabilised using heterobifunctional SH-PEG-COOH (5 kDa). The amount of PEG added to the nanoparticles was prepared in a 1:2 ratio (NPs:PEG) of the total weight of gold used in the synthesis. PEG was diluted in 1 mL Milli-Q and a determined volume of a 10 mg/mL stock solution of $NaBH_4$ was then added to reach 1:1 molar ratio of PEG:$NaBH_4$. The entire volume of the PEG-$NaBH_4$ solution was completely added to NPrs, and adjusted to pH 12 with 2 M NaOH under mild mixing. Finally, the solution was sonicated for 1 h at 60 ºC, and then centrifuged at 4,400 G for 15 min at room temperature to precipitate the NPrs and separate them from excess PEG and unreacted starting materials. Pellets were resuspended in Milli-Q water and centrifuged three times at 4,400 G for 9 min at room temperature. These final samples were diluted to one quarter of their original volume and aliquoted in 50 mL centrifuge tubes and allowed to rest at room temperature for several weeks. After this time the larger, heavier NPrs sediment at the bottom of the centrifuge tubes and the upper layer of the solution (containing the smaller, lighter polyhedral gold particles) could be removed.

2.2 Synthesis of gold nanorods (NRs)

A modified procedure, based on a previously reported seeded-mediated growth method [41], was used to prepare high aspect ratio gold nanorods, with LSPR bands higher than 1000 nm (Scheme 1b).

Seed solution: To prepare the seed solution a stock of 1 M $NaBH_4$ (aq) dissolved in 1 M NaOH (aq) was prepared and diluted 100 times in Milli-Q water, giving a final concentration of 0.01 M $NaBH_4$ in 0.01 M NaOH. Then, 5 mL 1 mM $HAuCl_4$ (aq) and 5 mL 0.2 M CTAB (aq) were mixed together. CTAB was dissolved to homogeneity in a water bath at 37 ºC. 460 µL of the previously prepared $NaBH_4$/NaOH stock solution was then added, resulting in a light-brown mixture within seconds, evidence of the presence of Au^0 seeds. This brownish mixture was allowed to stand for no more than a few minutes before use in the growth solution.

Growth solution: The growth solution was prepared by mixing 50 mL 1 mM $HAuCl_4$ and 50 mL 0.2 M CTAB solution, followed by the addition of 700 µL 0.1 M $AgNO_3$. Then 1 mL 0.5 M hydroquinone was added and the resulting mixture was stirred until the solution became clear. Finally, 1.6 mL seed solution was added. The growth reaction mixture was aged for 5 hours at 26 ºC in a water bath.

Washing and PEGylation of NRs

Several centrifugation-washing steps were required after each reaction to clean NRs from excess surfactant. In order to maintain the colloidal stability while obtaining PEG-stabilised NRs, various PEGylation steps were performed in between washing steps. Firstly, 5 mg of heterobifunctional HS-PEG-COOH (5 kDa) diluted in 1 mL Milli-Q water were added to 37 µL of a freshly made 1 mg/mL $NaBH_4$ (aq.) and left undisturbed for several minutes at room temperature. Then, the growth solution was centrifuged at 15,000 G, 15 min, 30 ºC, and pellets were resuspended in 100 mL Milli-Q water, followed by the addition of 1 mL of previously prepared PEG solution. Finally, the pH was raised by adding 100 µL of 1 M NaOH to the resultant solution (obtaining a pH value of 10.5 - 11) and the sample was aged overnight (20 h) at room temperature, trying to avoid that the temperature drops below 25 ºC to avoid CTAB crystallization. The next day, an identical PEGylation step was performed. The sample was centrifuged (15,000 G, 15 min, 30 ºC) followed by the resuspension of the pellets in 100 mL Milli-Q water to remove PEG excess and remaining CTAB from nanoparticles, and 1 mL of previously prepared PEG solution was added. The pH was raised again (obtaining a pH value of 10.5 - 11). The resulting mixture was then sonicated for 15 min

at 60 ºC, followed by another centrifugation at the same conditions to remove excess PEG. Pellets were resuspended in 100 mL Milli-Q water and one last centrifugation was performed at the same conditions to concentrate the sample, which pellets were resuspended in a final volume of 15 mL in Milli-Q water. Samples were stored at room temperature and the concentration of nanorods was obtained applying a conversion factor of (ε) 74 mL mg^{-1} cm^{-1} at their LSPR (1044 nm). Note: ε was obtained from combined UV-vis spectroscopy/ICP analyses.

2.3 Characterisation of nanoparticles

All the nanostructures used in these studies were characterised by SEM and TEM imaging, UV-Vis spectroscopy and ICP. The heating power of the nanoparticles was measured, to obtain heating curves for each type of nanoparticle.

Heating curves

The heating capability was measured applying a homogeneous non-dispersed and fully collimated laser beam adjusted to the bottom area of one single well on each irradiation (96-well-plates). To avoid pre-heating adjacent samples by both diffraction of the beam and/or by heat diffusion, one empty well was located in between samples. All samples were irradiated at 1100 mW for 10 min and reproduced in triplicates to obtain mean values and standard deviation errors. The temperature probe was washed and cooled down in Milli-Q water before collecting new data. Note that, prior to these measurements, the NPs were incubated in DMEM medium for 24 hours (37 ºC, 5 % CO_2) in order to simulate cell culture conditions, and to provide additional information about possible changes in their size and/or shape that may affect their optical properties, stability and so forth. Conformational changes were monitored using UV-Vis and SEM imaging during the process.

Each concentrated stock of NPs was mixed with DMEM to a final volume of 300 μL per well, giving a final concentration of ~20, 100, 120, and 150 μg/mL for NPrs, and of ~20 and 100 μg/mL for NRs. To be able to correlate the heating curves of these experiments to the conditions used for cell irradiation, the final volume contained no more than 10 % water. These 300 μL were loaded into each well. Blank was performed irradiating 300 μL of DMEM. Plates were incubated 24 h under culture conditions (37 ºC, 5 %

CO_2). All measurements were performed under the working laser configuration described previously, keeping the plate at 37 ºC inside a plate heater. The solution temperature was registered every 5 seconds during the irradiation for a total of 10 min.

These heating curves were also used to calculate the heating capacity and efficiency of both nanoparticles at the studied concentrations. For this purpose, a linear regression of the heating curves during the first 30 seconds of irradiation was calculated in order to obtain the temperature increase per second. The specific heat and density values of the DMEM were approximated to those of water and the heat needed to produce this temperature increase in each well was determined. The heating efficiency was calculated using these heat values and the laser power of 1100 mW.

2.4 Vero cell line internalisation studies

Optical microscopy internalization studies

Vero cell line (kidney epithelial cells from African green monkey) were acquired from the American Type Culture Collection (ATCC: CCL-81). Cells were cultured at 37 ºC in a 5 % CO_2 atmosphere in Dulbecco's modified Eagle's medium (DMEM) supplemented with 10 % foetal bovine serum (FBS), 2 mM glutamine and 100U /mL penicillin/streptomycin.

For the preparation of the samples of fixed cells for Dark Field microscopy visualization, $5x10^4$ Vero cells/well were seeded on a glass coverslide placed in a 24-multiwell plate and grown overnight under standard cell culture conditions (37 ºC, 5 % CO_2). The following day, nanoparticles in DMEM at the optimised concentrations (NR20, NR100 and NPr100, *see results and discussion section*) were added to each well and incubated for 24 hours (V_f H_2O <10 %). Cells were washed four times with DPBS, fixed in 4 % paraformaldehyde for 20 minutes at 4 ºC, washed twice with DPBS and incubated for 10 minutes with DAPI for nuclei labelling. The coverslips were mounted on glass microscope slides using 6 µL of Prolong® Diamond Antifade Mountant from Life Technologies®.

ICP internalisation studies

$5x10^4$ Vero cells were seeded in a 24-multiwell plate and grown overnight under standard cell culture conditions (37 ºC, 5 % CO_2). Afterwards, the medium was removed and nanoparticles in DMEM at

selected concentrations were added: NR20, NR100 and NPr100 (*see results and discussion section*). The cells were left for 24 h incubating with nanoparticles to allow their internalization. In the case of the control cell samples (cells without nanoparticles for cell counting and for blank subtraction) the medium was replaced with fresh one. Following, cells were washed thoroughly with PBS and trypsinized. Afterwards cells were transferred to Eppendorf vials for acid digestion. Control cells were counted using Trypan Blue. To digest the samples, cell pellets (of blank cells, cells with NR20, NR100 and NPr100) together with 100 % sample of NR20, NR100 and NPr100 were treated with 100 µL of Piranha solution (3:1 sulfuric acid, 96 % : hydrogen peroxide, 33 %) for 15 min at room temperature followed by 300 µL *aqua regia* (1 : 3 nitric, 65 % : hydrochloric acid, 37 %) for 2 h at room temperature. Subsequently the samples were incubated at 60 ºC for 15 min and diluted with Milli-Q water to 20 mL. All samples were performed in duplicate and evaluated by ICP-AES and/or ICP-MS.

Intracellular location of NPs

To determine the intracellular localization of the AuNPs, cells were analysed via TEM. $2x10^4$ Vero cells were seeded in an 8-well chamberslide (permanox, Nunc) and incubated 24 h under standard cell culture conditions. Thereafter, cells were incubated for 24 h with the optimised concentration of NRs and NPrs (in this case NR100 and NPr100, *see results and discussion section*). Then, cells were washed with PBS to remove free nanoparticles and fixed with 2.5 % glutaraldehyde in 0.1 M phosphate buffer (PB) for 1 h at 4 ºC. Afterwards, the cells were washed four times with 0.1 M PB to remove glutaraldehyde. Samples were then post-fixed with 2 % osmium tetroxide, rinsed, dehydrated and embebed in Durcupan resin (Fluka, Sigma-Aldrich, St. Louis, USA). 1.5 µm semi-thin sections were cut with an Ultracut UC-6 (Leica, Heidelberg, Germany) and stained with 1 % toluidine blue. Finally, ultra-thin sections (0.08 µm) were cut with the microtome, stained with lead citrate (Reynolds solution) and examined under a 200 KeV FEI Tecnai T20 (FEI Europe, Eindhoven, Netherlands) operating at 80 KeV.

2.5 Irradiation of Vero cells with NIR-laser

Thermoablation

Vero cells were seeded at a density of $5x10^3$ cells per well in a 96-multiwell plate and incubated under cell culture standard conditions. After 24 hours the medium was replaced for fresh DMEM with the desired concentrations of each nanoparticle (NR20, NR100 and NPr100, *see results and discussion section*) and incubated for another 24 hours under the same conditions (V_f H_2O <10 %). Thereafter, the medium was removed, the cells were washed twice with DPBS to remove any excess of non-internalized particles or dead cells and a fresh phenol red-free DMEM was added. Plates were irradiated under working laser configuration for 10 min, with temperature control set up to 37 ºC. Samples were performed in triplicate. Non-irradiated samples of cells with and without NPs, together with irradiated cells (without NPs) were used as controls. The heat produced by the NPs was registered after 10 min laser irradiation with a fibre optic thermometer. The morphological changes of the cells were carefully monitored using phase-contrast microscopy at several intervals post-irradiation on a Nikon Eclipse Ti microscope and representative images were collected five hours post-irradiation.

MTT cell viability assays

In a separate experiment, the conditions were reproduced in order to quantify the viability of the cells by MTT assay. The cells were irradiated with the NIR laser at the same conditions described previously and incubated for 5 hours under cell culture conditions. Then the medium was removed and the cells were incubated with 200 µL of DMEM containing 10 µL of 5 mg/mL MTT in the dark under culture conditions for 105 minutes. During this time, a yellow tetrazole MTT dye is converted into violet formazan crystals by the NAD(P)H-dependent succinate dehydrogenase, a mitochondrial enzyme in living cells. Finally, the plate was centrifuged at 2,500 rpm for 30 minutes, the supernatant was removed and the formazan crystals were solubilised with 100 µL of dimethyl sulfoxide (DMSO). After a proper resuspension of the crystals, the optical density at 555 nm was recorded using a plate reader.

Comentario [JdlF1]: Cuantas?

Comentario [JdlF2]: Poner todo en g

Comentario [JdlF3]: Poner la fórmula de como se caluula

3. Results & Discussion

3.1 Synthesis of nanoparticles

NPrs with an LSPR band at *ca.* 1100 nm (as close as possible to the wavelength of the NIR laser, 1064 nm) were synthesised using an adaptation of a previously reported procedure [22]. Sodium thiosulfate

$Na_2S_2O_3$ (aq) was used as a mild reducing agent for gold salt chlorauric acid ($HAuCl_4$). The principal modifications of this synthetic procedure were i) the addition of potassium iodide, KI (12.2 μM final concentration) and ii) that the Au^{3+} to Au^0 reduction was performed in three time-lapsed steps, as opposed to two steps, allowing NPrs "seeds" to form and grow (Scheme 1a). The synthesis of NRs with high aspect ratio was performed following a seed-mediated growth process thoroughly described in the literature [31,41,43] (Scheme 1b). After several unsuccessful attempts to synthesise NRs in high yield with LSPR band >1000 nm, we identified a highly reproducible procedure and amended it to suit our requirements [41]. For our purposes, this protocol was adapted by some minor modifications and scaled-up (x10). Notably, the most significant of these alterations to the published synthetic procedure was that the reaction (the 'growth solution') was carried out at 26 ºC in a water bath to avoid CTAB crystallisation. The reaction was incubated in the water bath for five hours, until the LSPR wavelength reached a maximum [41,42] of *ca.* 1080 nm.

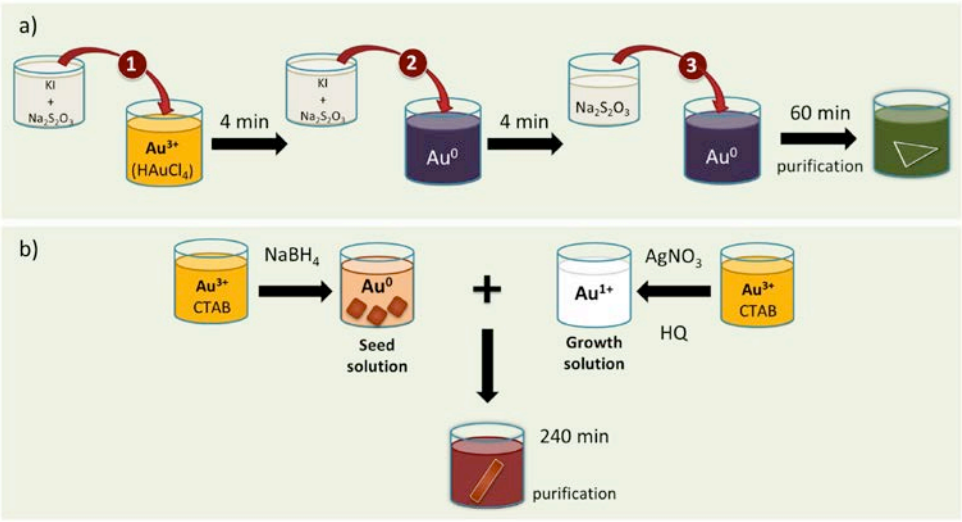

Scheme 1 – Step-by-step representation of the synthesis of the nanoparticles; a) synthesis of gold nanoprisms (NPrs); b) synthesis of gold nanorods (NRs).

To further increase the colloidal stability of the nanoparticles, all the reaction products were derivatised with heterobifunctional polyethylene glycol (HS-PEG-COOH, MW = 5000 g/mol (5 kDa)) [36]. An excess of the polymer was added to the NPs solution to saturate the nanoparticle surface and ensure fully stabilised

nanostructures [22]. To avoid the formation of S-S bonds between individual PEG molecules (PEG dimers) sodium borohydride, $NaBH_4$, was required as a reducing agent at a molar ratio of 1:1 with PEG at pH 12.

The PEG stabilisation of the NPrs was carried out under sonication of the mixture at 60 ºC for one hour to speed-up the process, and as an alternative to the reported over-night incubation under mild mixing [22]. A final centrifugation step was performed in order to discard excess of reagents; thereafter the samples were allowed to rest at room temperature for several weeks to sediment and separate the heavier NPrs from smaller pseudo-spheres and other pollutants remain in the upper phase.

On the other hand, surfactants (CTAB) on the surface of NRs exist in a dynamic equilibrium with the media, attached by non-covalent mostly hydrophobic interactions [38,41]. By removing as much supernatant as possible at these steps it is possible to change that dynamic balance in our favour, decreasing the amount of CTAB on NR surface that helps PEG to successfully reach the gold surface and form a conjugated stronger bond thanks to its thiol groups, while at the same time keeping the NRs stable in a CTAB-depleted medium. Taking into account that increasing centrifugation velocity may lead samples to undergo non-desirable shift in their longitudinal plasmonic wavelengths and aggregation, the only way to carry out a well performed washing step was to increase the centrifugation times. An optimised washing-stabilisation protocol was performed by adding two partial PEG stabilisations between each of the last centrifugation steps, the last of which is thereafter sonicated in order to enhance the PEGylation process, giving a LSPR peak at 1044 nm at the end of the PEGylation process.

3.2 Characterisation of nanoparticles

Both types of nanoparticles were characterised by ICP, UV-Vis, TEM and SEM (Figures 1 and S1). The UV-Vis spectra of both types of NP showed their LSPR bands to be well inside the NIR range (1044 nm for NR@PEG and 1100 nm for NPr@PEG) and with sufficient overlap with the NIR laser (Figure 1). Correlating the LSPR absorbance obtained by UV-Vis spectroscopy with the Au concentration obtained from ICP analysis it was possible to obtain a conversion factor (ε) of 29 mL mg^{-1} cm^{-1} for NPrs and 74 mL

mg^{-1} cm^{-1} for NRs for calculating weight concentration (mg/mL) of gold NPs in each sample. The respective yields for each synthesis were 71 % for the NPrs and 80 % in the case of NRs (Figure 1c). Both types of NPs also showed a strong absorbance peak at ~530 nm corresponding to a combination of NPs transversal absorbance and pseudo-spherical polyhedral gold nanoparticles. Comprehensive TEM and SEM analyses were used to calculate the surface area of the particles. NPrs (considered as triangular prisms with 173 nm side and 9 nm constant thickness [22]) possess a surface area of 15.0 m^2/g; while NRs (considered as perfect cylinders of 11 nm diameter and 76 nm length, Figure 1c) have a surface area of 23.2 m^2/g.

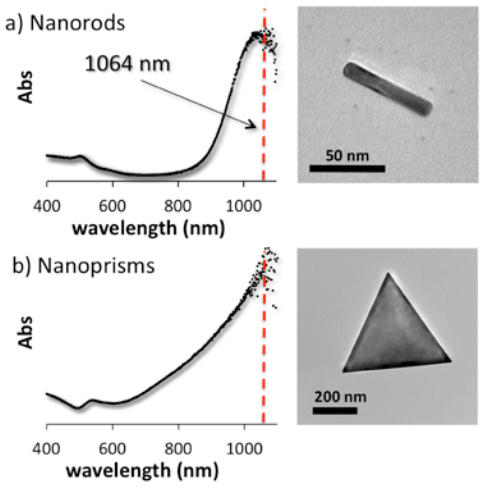

c)

	Yield	Length (nm)	Width (nm)	Surface area (m^2/g)
NPrs	70,7%	173	9	15,0
NRs	79,7%	76	11	23,2

Figure 1 – UV-Vis spectroscopy, TEM images and characteristic size and surface area of the particles. a) NRs and b) NPrs. Red dotted lines represent the wavelength of the NIR laser (1064 nm). Both nanoparticles possessed a dominant LSPR band in the NIR range overlapping with the wavelength of the laser, 1064 nm. c) From left to right: reaction yield; length, width and surface area of each type of nanoparticle.

TEM: Transmission Electron Microscopy; NRs: Gold Nanorods; NPrs: Gold Nanoprisms; NIR: Near Infra-Red.

3.3 Optimisation of heating conditions

Several heating trials were performed to evaluate the heating capacity of both types of AuNPs upon laser irradiation. The NRs were found to be far more effective light-to-heat transducers, presumably owing to their higher specific surface area. Thus, an increasing concentration of NPrs was tested (from ~20 to 150 μg/mL) in order to identify the concentration of NPrs that showed the same heating capacity as NRs. For these studies, two standard concentrations of NRs were used (*ca*. 20 and 100 μg/mL, herein referred to as NR20 and NR100, respectively) (Figure 2). The results revealed a linear relation of initial heating power with concentration, for both the NRs and NPrs (Figure S2). In these initial studies, NPr100 (100 μg/mL) heated at a rate of 0.30 ºC/s and gave a final temperature of 87.9±7.8 ºC after 10 min irradiation, which was similar to NR20 (0.25 ºC/s and 83.6±6.9 ºC) (Figure 2). These concentration values (NR20 and NPr100) for each nanoparticle type were selected for further analysis as both revealed similar heating capabilities, with only minor deviation.

These optimum concentrations were then also compared with the heating of NR100 (*ca*. 100 mg/mL) in order to have a direct comparison of the effect with respect to the weight of gold for each nanoparticle type. NR100 displayed the greatest heating effect, characterised by an initial rate of 0.40 ºC/s and a final irradiation temperature of 93.3±6.3 ºC, as well as the highest heating efficiency, transforming 45.3 % of the laser light intensity (1100 mW) at the plate into heat to increase the temperature of the sample with a power of 498 mW. This higher heating capacity of the NRs correlates with the higher absorbance intensity of the LSPR peak observed by UV-Vis. At the other end of the scale, NPr20 showed an initial rise in temperature of 0.17 ºC/s and reached 68.3±4.5 ºC after 10 min. The intrinsic heating of the DMEM control should be noted (0.06 ºC/s and 42.2±3.3 ºC) and that such effects are often observed in photothermal therapy applications [39].

a) Temperature rise during 10 min laser irradiation

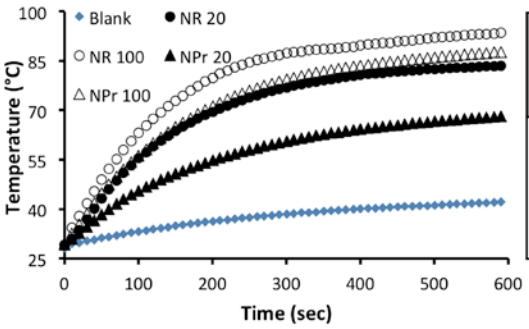

b) Summary of heating properties

Sample	Temperature Increase (°C/s)	Heating Efficiency (%)	Temperature after 10 min irradiation (°C)
Blank	0,06	6,92	42,2±3,3
NR20	0,25	29,03	83,6±6,9
NR100	0,40	45,27	93,3±6,3
NPr20	0,17	19,54	68,3±4,5
NPr100	0,30	34,03	87,9±7,8

Figure 2 – Characterisation of the heating capacity. The heating ramps (a) represent the rise in temperature registered by each type of nanoparticle during the 10 min irradiation period. The table (b) represents, from left to right: heating efficiency as the representation of the slope of the curve during the first 30 seconds of irradiation, the % of laser intensity that is effectively converted into heat, and the final temperature reached after 10 min laser irradiation.

Thus, NR20 and NPr100 (concentrations 20 and 100 μg/mL, respectively) have been selected for further cellular studies as they displayed approximately the same overall heating capacities after 10 minutes irradiation. In addition to basing our observations on the heating effect of the particles we also wanted to have a direct comparison for the concentration of Au, therefore NR100 (100 μg/mL) was also included in the following study since they possess the same concentration of Au as NPr100.

UV-Vis spectroscopy and SEM imaging before and after the 10-min period of irradiation period was used to examine the stability of the NPrs and NRs. Neither the NP morphology nor the LSPR bands were affected by the laser irradiation (Figure S3). The apparent increase in the intensity of the LSPR band after irradiation is caused by the evaporation of water which leads to a subsequent increase of the effective concentration of the particles in solution. Some studies suggest that laser irradiation can change and deform NP shape altering the physicochemical properties of the material [40,42]. Our results demonstrate

that for the conditions tested herein, this is not the case and the NPs retain their shape, LSPR properties and colloidal stability.

At this point in our analysis, the higher yield, surface area and heating efficiency all greatly favour the NRs over the NPrs as photothermal agents; but to delve deeper into this comparison, *in vitro* analyses comparing these particles were necessary.

3.4 Cellular internalisation studies

Several cellular internalisation studies were performed (bright field, dark field, TEM microscopy and ICP analysis) using the selected concentrations of NPs (NR20, NR100 and NPr100).

Since AuNPs produce insufficient contrast to be visualized by bright field microscopy alone, the precise location of the NPs within the cells was obtained using resin-bound cells that were cut with a microtome into ultra-thin slices and stained for electron microscopy investigations. Vero cells were incubated for 24 h with the two samples that contained the same concentration of Au, NR100 and NPr100, prior being fixed with glutaraldehyde, post-fixed with osmium tetroxide and embedded in Durcupan resin. Semi-thin 1.5 µm sections were cut into finely into ultra-thin sections of <0.08 µm. Samples were stained lightly with toluidine blue for TEM imaging. A reference Vero cell sample was left untreated as a control. Both NRs and NPrs accumulated inside vesicles and none appeared attached to the plasma membrane, free in the cytoplasm or in the nucleus (Figure 3). With this technique, the higher level of internalisation of NPrs than of NRs was clearly evident, but not quantifiable.

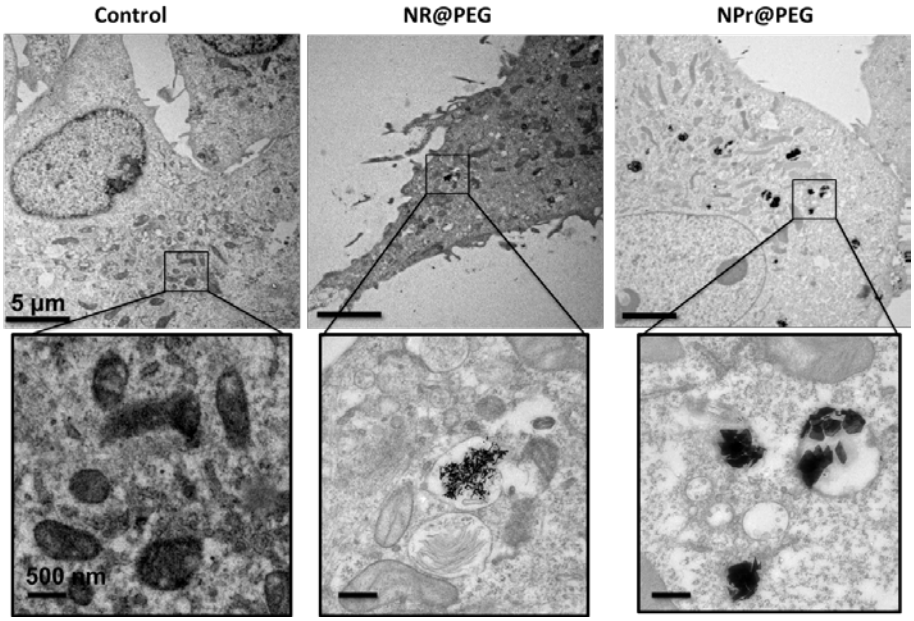

Figure 3 – Subcellular localisation of nanoparticles. TEM imaging of ultra-thin slices of fixed cells following 24 hours incubation with NRs or NPrs. AuNPs were distributed inside vesicles; no AuNPs were observed inside the nucleus or attached to the cytoplasmic membrane.

TEM: Transmission Electron Microscopy

From these images we postulated that there was a greater internalisation of NPr than NRs as there were more vesicles containing NPr, but to gain a better understanding of this we used ICP analysis to quantify the internalisation of Au inside the cells. In a separate experiment, after 24 h incubation of Vero cells with NR20, NR100 and NPr100 concentrations, the amount of internalised gold in the samples was measured by ICP analysis. The data showed that while the concentration of NR100 internalized in Vero cells was equal to 0.077 pg of Au/cell, the concentration of internalised NPr100 reached 28.73 pg Au/cell, i.e. >370 times higher than for NR100. The extremely low concentration of NR20 inside cells equalled 0.021 pg of Au/cell, which was commensurate with particle-free controls, i.e. the internalisation was considered to be essentially non-existent.

Finally, the AuNP internalisation was analysed by dark field microscopy/fluorescence (DAPI) (Figure S4). As ICP failed to show any significant NR20 internalisation we opted to assess only the highest NP concentrations (100 mg/mL), just as for the TEM analysis. NR100 showed no observable internalisation, but NPr100 was clearly visible using dark field microscopy. This is probably caused by a combination of the higher contrast capability of NPrs coupled with the larger internalisation, thereby making dark field microscopy a practical and straightforward technique to assess the cellular internalization of NPrs, without being obliged to resort to other more complex and costly analytical techniques, such as TEM imaging of ultrathin sections or ICP analysis.

3.5 Irradiation of Vero cells with NIR-laser

Following determination and quantification of the intracellular location of the NRs and NPrs their heating effect *in vitro* was characterised. Vero cells were incubated with the previously studied concentrations of NR100 and NPr100 in 96-well plates for 24 hours and, only after removing the non-internalised NPs, the cells were irradiated for 10 minutes under the established working laser configuration. The thermoablation capacity of the concentration of NR20 was not analysed since ICP analyses were unable to detect a sufficient amount of gold to distinguish NR20 from the blank background, thus resorting to testing NR100. The laser intensity (3.3 W/cm^2) was kept intentionally low during both the heating characterisation and throughout the cell irradiation process in order to stay in the range where cell death is mainly governed by an apoptotic process, according to recent studies [15]. A fibre optic thermometer was used to measure the temperature rise upon laser irradiation and cell death was monitored by phase-contrast microscopy post-irradiation to determine the optimal point for cell viability assays (Figure 4b). Consequently, at five hours post-irradiation, MTT cell viability assays were performed (Figure 4a). The results derived from the MTT assays shown that, although NR100 and NPr100 concentrations were essentially non-toxic to the Vero cell line before irradiation, applying the laser to cells with NR100 reduced viability to 86±3 %; while in the case of NPr100 viability was reduced to 44±1 %. Importantly, the irradiated particle-free control cell viability stood at 92±5 %, revealing that the laser itself is not able of inducing significant cell death under the studied conditions. Phase-contrast microscopy of the cells at five-hours post-irradiation aptly illustrate how the cells incubated with NPr100 are apoptotic/necrotic; whereas cells treated with NR100 show

morphology commensurate with the control cells (Figure 4b). Analysis of final cell culture temperatures following 10 minutes irradiation showed that the net temperature rises for the same NP concentrations (NPr100 and NR100), one can observe how NPr100 reached 47 ºC while NR100 reached 45 ºC. It is important to note that the global temperature of the Vero cells without particles reached 43 ºC indicating that cultured cells do display some interaction with the 1064 nm laser beam.

The *in vitro* studies show that only NPr100 was capable of inducing cell death upon irradiation, and at the same time raises the global temperature of the medium higher than NR100. These results are consistent with the higher internalisation levels of the NPrs inside the cells observed in the ICP analyses. Although NRs provide a more efficient light-to-heat conversion, we have observes poor cellular internalisation, making them incapable of inducing cell death under the conditions employed in this study. It should be noted that many studies on AuNRs for photothermal therapy applications often employ higher concentrations of AuNRs and long irradiation times [39], whereas we routinely aim to employ the minimum required concentration to induce cell death [15,43]. Furthermore, AuNRs are frequently used as platforms for multi-therapeutic modalities so have vastly more complex surface functionalities than our simple PEG-stabilised NRs, for example mesoporous silica shell around the NR [44]. Thus the combination of low particle concentrations with a simple passivized polymer surface may account for the poor cellular internalisation and subsequent low cytotoxicity of the NRs under laser irradiation.

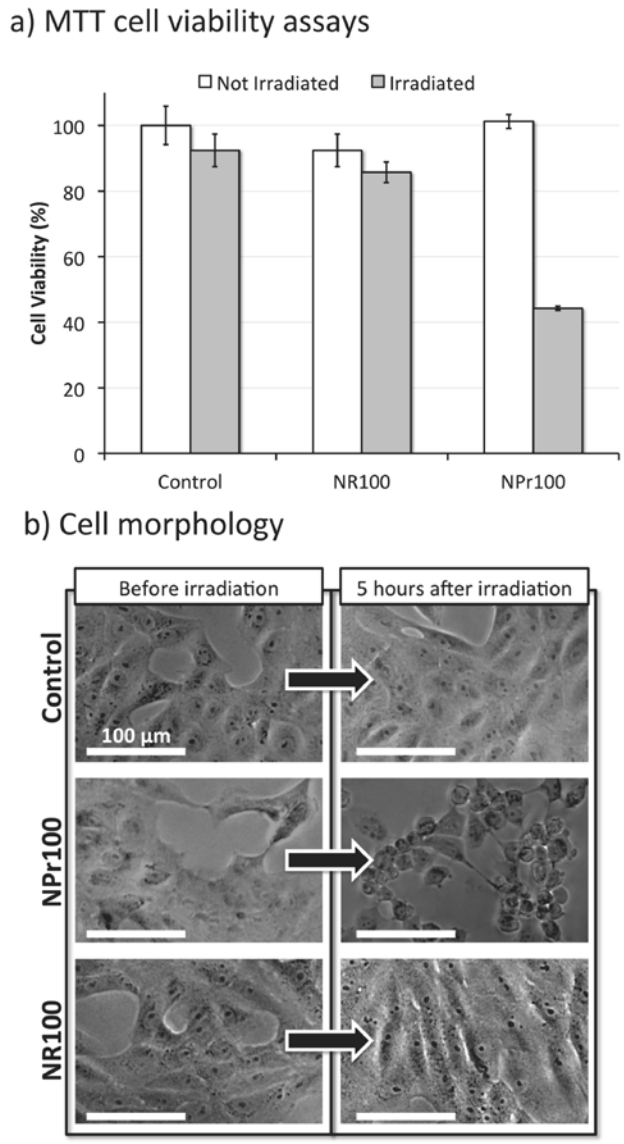

Figure 4 – Cell viability and morphology following thermoablation studies. (a) MTT assays for cell toxicity and viability of NR100 and NPr100 (100 µg/mL) of irradiated and non-irradiated cell samples. (b) Cell morphology changes post-irradiation: cells incubated with NR100 and NPr100 were observed by phase-contrast microscopy for five hours post-irradiation; all scale bars correspond to a distance of 100 µm; neither irradiation of nanoparticle-free control nor NR20 (~20 µg/mL) revealed changes in cell

morphology; however, cells incubated with NPr100 (~100 µg/mL) began showing significant morphological changes from two hours post-irradiation and peaked at five hours.

4. Conclusions

In summary, our group is interested in biomedical applications of AuNPs involving the exploitation of their efficient light-to-heat transduction upon excitation of their LSPR band. Here we have demonstrated how two types of anisotropic AuNPs can be synthesised and adapted to our needs. The LSPR bands of gold nanoprisms (NPrs) and nanorods (NRs) were adjusted to absorb close to the wavelength of the NIR laser (1064 nm) so that these particles could be evaluated and compared as photothermal agents. From the evaluation of the nanoparticles to serve as light-to-heat transducers, both types of nanoparticles revealed excellent light-to-heat conversion. Cellular internalisation studies with Vero cell line revealed that the NPs were essentially non-toxic at the tested concentrations and were located inside cytoplasmic vesicles.

Although both NPrs and NRs showed a high heating efficiency, NRs stand out as being more efficient, largely due to their higher specific surface area. However, ICP and TEM studies led us to conclude that NPrs internalise more efficiently than NRs. The effect of the increased internalisation means that for NIR-irradiation of cells incubated with these nanoparticles at the same weight concentration, only the NPrs possessed capability to induce cell death, under the conditions tested herein. These observations, in conjunction with the less practical and time-consuming multi-step synthetic method required to obtain a sufficient amount of NRs for reliable cell studies, lead us to conclude that NPrs are more appropriate candidates for *in vitro* cellular thermoablation.

Future perspective

In the first instance, the size and shape of photothermal materials are the primary drivers of their unique properties. Nevertheless, the individual light-to-heat conversion efficiencies and cellular internalization capabilities of each type of particle significantly broadens potential downstream application, since these processes ultimately govern the biological application of nanoparticles. Our research has led us to begin to

focus with more intent on understanding the subcellular processes at play during the use of nanoparticles as photothermal agents [15,43,44].

A wide variety of methodologies are published describing various types of anisotropic AuNPs that would be applied in optical hyperthermia therapies for the fight against cancer, above many other potential applications. As a result of the vast range of shapes, sizes, physicochemical properties, surface functionalities and other characteristics of these NPs, it is important to carry out comprehensive comparative studies of to determine which type of particle best meets a specific purpose.

Future studies include gaining a deeper understanding of the mechanisms by which each type of NP is internalised by the cells (caveolae, clathrin-mediated…) [45]. The kinetics of cellular internalisation using a combination of ICP, confocal and dark field microscopies will provide additional information on the cellular internalisation mechanisms. In this way, we might understand the cause by which NPrs are being internalised in higher amounts than NRs. We are currently investigating gene expression as a result of the photothermal therapy treatment (hsp70, apoptosis-related genes…) to provide guidelines for which particles are more lethal to specific types of cancer and are performing *in vivo* cytotoxicity screening and nanoparticle fate in mice.

Summary points

Synthesis and characterisation of nanoparticles

- Non-toxic PEG-covered rod-shaped and prism-shaped gold nanoparticles were synthesised to possess LSPR bands in the NIR range, *ca.*1064 nm.
- Neither NRs nor NPrs suffered from morphological changes under the working laser configuration, these particles are entirely stable under our experimental conditions.
- Although both nanoparticles acted as efficient light-to-heat transducers, a lower concentration of NRs (by weight, μg/mL) is required to produce the same amount of heat as NPrs.

Cellular internalisation

- It was not possible to detect any type of particle by phase contrast microscopy. However, NPrs can easily be detected by dark field microscopy, which makes this method a quick and practical means of detecting NPrs in cells or tissues.
- TEM images of ultra-thin slices of NPs internalised within cells showed that both types of NP were located inside cytoplasmic vesicles, and there were no traces of particles attached to either the cell membrane or the nucleus.
- ICP analysis was used to quantify the cellular internalisation these nanoparticles, revealing how NPrs internalised more effectively (>370 times more) than NRs in the Vero cell-line.

Cell death by thermoablation

- The laser irradiation conditions had no detrimental effect on cells in the absence of NPs.
- The dose of NPs applied was harmless to the cells before irradiation.
- Thermoablation studies proved that NPrs were more effective in intracellular heat production at a given concentration of both nanoparticles (~100 μg/mL).
- Only NPrs were able to induce cell death under the studied conditions.
- The cellular internalisation capacity of the NPs is therefore a key factor for any subsequent photothermal application.

References

Those publications of special relevance have been highlighted as: * of interest; ** of considerable interest.

1. Vigderman L, Khanal BP, Zubarev ER. Functional gold nanorods: synthesis, self-assembly, and sensing applications. *Adv. Mater.* 24(36), 4811–4841, (2012).

   * General understanding review of synthesis of nanorods and their plasmonic properties.

2. Green HN, Crockett SD, Martyshkin DV, *et al.* A histological evaluation and in vivo assessment of intratumoral near infrared photothermal nanotherapy-induced tumor regression. *Int. J. Nanomedicine* 9, 5093–5102 (2014).
3. Wang Y, Black KCL, Luehmann H, *et al.* Comparison Study of Gold Nanohexapods, Nanorods, and Nanocages for Photothermal Cancer Treatment. *ACS Nano,* 7(3), 2068–2077 (2013).
4. Liu J, Detrembleur C, Grignard B, *et al.* Gold nanorods with phase-changing polymer corona for remotely near-infrared-triggered drug release. *Chem. Asian J.* 9(1), 275–288 (2014).
5. Huschka R, Barhoumi A, Liu Q, Roth JA, Ji L, Halas NJ. Gene silencing by gold nanoshell-mediated delivery and laser-triggered release of antisense oligonucleotide and siRNA. *ACS Nano* 6(9), 7681–7691 (2012).
6. Conde J, M de la Fuente J, Baptista PV. Nanomaterials for reversion of multidrug resistance in

cancer: a new hope for an old idea? *Front. Pharmacol.* 4, 134 (2013).

7. Bao C, Beziere N, del Pino P, *et al.* Gold nanoprisms as optoacoustic signal nanoamplifiers for in vivo bioimaging of gastrointestinal cancers. *Small* 9(1), 68–74 (2013).
8. Han J, Zhang J, Yang M, Cui D, M de la Fuente J. Glucose-functionalized Au nanoprisms for optoacoustic imaging and near-infrared photothermal therapy, *Nanoscale*, 8, 492-499 (2016).
9. Polo E, del Pino P, Pelaz B, Grazu V, M de la Fuente J. Plasmonic-driven thermal sensing: ultralow detection of cancer markers. *Chem. Commun.* 49(35), 3676–3678 (2013).
10. Mayer KM, Hafner JH. Localized surface plasmon resonance sensors. *Chem. Rev.* 111(6), 3828–3857 (2011).
11. Bao C, Conde J, Polo E, del Pino P, Moros M, Baptista PV, Grazu V, Cui D, M de la Fuente J. A promising road with challenges: where are gold nanoparticles in translational research? *Nanomedicine* 9(15), 2353–2370 (2014).
12. Dreaden EC, Mackey M, Huang X, Kang B, El-Sayed M. Beating cancer in multiple ways using nanogold. *Chem. Soc. Rev*. 40(7), 3391–3404 (2011).
13. Yin Z, Zhang W, Fu Q, *et al.* Construction of Stable Chainlike Au Nanostructures via Silica Coating and Exploration for Potential Photothermal Therapy. *Small* 10(18), 3619–3624 (2014).
14. Dreaden EC, Alkilany AM, Huang X, Murphy CJ, El-Sayed M. The golden age: gold nanoparticles for biomedicine. *Chem. Soc. Rev.* 41(7), 2740–2779 (2012).

    * Comprehensive review that summarises most of the knowledge about gold nanoparticles, their nature, properties, potential applications and drawbacks, together with several references about how to solve them.

15. Perez-Hernandez M, del Pino P, Mitchell SG, *et al.* Dissecting the molecular mechanism of apoptosis during photothermal therapy using gold nanoprisms. *ACS Nano* 9(1), 52–61 (2015).

    ** Core article that thoroughly describes the intracellular processes that carry out inside the cells during thermoablation, as well as the irradiation protocol on which our studies are based.

16. Mishra R, Welsh RM, Szomolanyi-Tsuda E. NK Cells and Virus-Related Cancers, *Crit. Rev. Oncog*. 19(0), 107–119 (2014).
17. Jiang K, Smith DA, Pinchuk A. Size-Dependent Photothermal Conversion Efficiencies of Plasmonically Heated Gold Nanoparticles. *J. Phys. Chem. C* 117(51), 27073–27080 (2013).
18. Reddy LH, Arias JL, Nicolas J, Couvreur P. Magnetic nanoparticles: design and characterization, toxicity and biocompatibility, pharmaceutical and biomedical applications. *Chem. Rev.* 112(11), 5818–5878 (2012).
19. Fratila RM, Mitchell SG, del Pino P, Grazu V, M de la Fuente J. Strategies for the biofunctionalization of gold and iron oxide nanoparticles. *Langmuir* 30(50), 15057–15071 (2014).
20. Ladj R, Bitar A, Eissa M, *et al.* Individual inorganic nanoparticles: preparation, functionalization and in vitro biomedical diagnostic applications. *J. Mater. Chem. B* 1(10), 1381-1396 (2013).
21. Rao CNR, Ramakrishna Matte HSS, Voggu R, Govindaraj A. Recent progress in the synthesis of inorganic nanoparticles. *Dalton Trans.* 41(17), 5089–5120 (2012).
22. Pelaz B, Grazu V, Ibarra A, *et al.* Tailoring the synthesis and heating ability of gold nanoprisms for bioapplications. *Langmuir* 28(24), 8965–8970 (2012).

    ** A core paper that describes the synthesis of gold nanoprisms together with an in-depth characterisation and the potential applications of these particles.

23. Dinish US, Goh D, Fu CY, Bhuvaneswari R, Sun W, Olivo M. Optimized Synthesis of PEG-

Encapsulated Gold Nanorods for Improved Stability and Its Application in OCT Imaging with Enhanced Contrast. *Plasmonics* 8(2), 591–598 (2012).

24. Pelaz B, Charron G, Pfeiffer C, *et al.* Interfacing engineered nanoparticles with biological systems: anticipating adverse nano-bio interactions. *Small* 9(9-10), 1573–1584 (2013).

25. Sapsford KE, Algar WR, Berti L, *et al.* Functionalizing nanoparticles with biological molecules: developing chemistries that facilitate nanotechnology. *Chem. Rev.* 113(3), 1904–2074 (2013).

26. Xiaoying Z. Gold Nanoparticles: Recent Advances in the Biomedical Applications. *Cell Biochem. Biophys.* 72(3), 771-775 (2015).

27. Walsh MJ, Barrow SJ, Tong W, Funston AM, Etheridge J. Symmetry Breaking and Silver in Gold Nanorod Growth. *ACS Nano* 9(1), 715–724 (2015).

28. Liz-Marzán LM. Tailoring surface plasmons through the morphology and assembly of metal nanoparticles. *Langmuir* 22(1), 32–41 (2006).

29. Stewart ME, Anderton CR, Thompson LB, *et al.* Nanostructured plasmonic sensors. *Chem. Rev.* 108(2), 494–521 (2008).

30. Shi W, Casas J, Venkataramasubramani M, Tang L. Synthesis and Characterization of Gold Nanoparticles with Plasmon Absorbance Wavelength Tunable from Visible to Near Infrared Region. *ISRN Nanomater.* 2012, 1–9 (2012).

31. Huang Y. Low-level laser therapy: an emerging clinical paradigm, *SPIE Newsroom*, 2–4 (2009).

32. Kannadorai RK, Chiew GGY, Luo KQ, Liu Q. Dual functions of gold nanorods as photothermal agent and autofluorescence enhancer to track cell death during plasmonic photothermal therapy. *Cancer Lett.* 357(1), 152–159 (2014).

33. Zhang F, Lees E, Amin F, *et al.* Polymer-coated nanoparticles: a universal tool for biolabelling experiments. *Small* 7(22), 3113–3127 (2011).

34 Alkilany AM, Nagaria PK, Hexel CR, Shaw TJ, Murphy CJ, Wyatt MD. Cellular uptake and cytotoxicity of gold nanorods: molecular origin of cytotoxicity and surface effects, *Small* 5(6), 701-708 (2009).

35. Ambrosone A, del Pino P, Marchesano V, Parak WJ, M de la Fuente J, Tortiglione C. Gold nanoprisms for photothermal cell ablation in vivo. *Nanomedicine* 9(13), 1913–1922 (2014).

* A step forward in the application of gold nanoprisms as photothermal agents using an invertebrate model organism (*Hydra vulgaris*) as the *in vivo* system.

36 Soenen SJ, Manshian BB, Abdelmonem AB *et al.* The Cellular Interactions of PEGylated Gold Nanoparticles: Effect of PEGylation on Cellular Uptake and Cytotoxicity, *Part. Part. Syst. Charact.* 31(7), 794–800 (2014).

37. Moros M, Hernáez B, Garet E, *et al.* Monosaccharides versus PEG-functionalized NPs: influence in the cellular uptake. *ACS Nano* 6(2), 1565–1577 (2012).

38. Kinnear C, Dietsch H, Clift MJD, Endes C, Rothen-Rutishauser B, Petri-Fink A. Gold Nanorods: Controlling Their Surface Chemistry and Complete Detoxification by a Two-Step Place Exchange, *Angew. Chem. Int. Ed*. 52, 1934-1938 (2013).

* refer to research cited herewithin

39.* Hwang S, Nam J, Jung S, Song J, Doh H, Kim S. Gold nanoparticle-mediated photothermal therapy: current status and future perspective, *Nanomedicine* 9(13), 2003–2022 (2014).

40. Taylor AB, Siddiquee AM, Chon JWM. Below Melting Point Photothermal Reshaping of Single Gold Nanorods Driven by Surface Diffusion, *ACS Nano* 8(12),12071–12079 (2014).

41. Vigderman L, Zubarev ER. High-Yield Synthesis of Gold Nanorods with Longitudinal SPR Peak Greater than 1200 nm Using Hydroquinone as a Reducing Agent. *Chem. Mater.* 25(8), 1450–1457 (2013).

** Core paper that describes the synthesis of gold nanorods used in this article.

42. Jana NR, Gearheart L, Murphy CJ. Wet Chemical Synthesis of High Aspect Ratio Cylindrical Gold Nanorods. *J. Phys. Chem. B* 105(19), 4065–4067 (2001).

43. Melamed JR, Edelstein RS, Day ES. Elucidating the fundamental mechanisms of cell death triggered by photothermal therapy. *ACS Nano* 9(1), 6–11 (2015).

44. Shen S, Tang H, Zhang X, *et al.* Targeting mesoporous silica-encapsulated gold nanorods for chemo-photothermal therapy with near-infrared radiation. *Biomaterials* 34(12), 3150–3158 (2013)

* An article that served as inspiration to apply changes in the synthesis of gold nanorods in order to adjust their optical properties to our needs.

45 Moros M, Mitchell SG, Grazú V, M de la Fuente J. The fate of nanocarriers as nanomedicines in vivo: important considerations and biological barriers to overcome. *Curr. Med. Chem.* 20(22), 2759–2778 (2013).

Acknowledgements

This work was supported by Shanghai Jiao Tong University, Fondo Social de la DGA (grupos DGA), Ministerio de la Economía y Competitividad del Gobierno de España for the public founding of Proyectos I+D+I - Programa Estatal de Investigación, Desarrollo e Innovación Orientada a los Retos de la Sociedad (project n. SAF2014-54763-C2-2-R) and the ERC-Starting Grant 239931-NANOPUZZLE. For financial support SGM acknowledges the Fundación General CSIC (Programa ComFuturo), AA acknowledges the Ministerio de Educación, Cultura y Deportes for a FPU grant (FPU014/06249) and MM acknowledges the European Commission for a MCSA Fellowship (Grant Agreement No. 660228). We wish to thank The Advanced Microscopy Laboratory (INA-Universidad de Zaragoza) for access to their instrumentation and expertise. We also gratefully acknowledge J. C. Raposo of the Servicio Central de Análisis de Bizkaia from SGIker of Universidad del País Vasco (EHU) for the ICP technical support. We also thank F. Luvi and A. Bird for fruitful discussions.

Con formato: Inglés (Estados Unidos)

SUPPORTING INFORMATION

"Gold Nanoprism-Nanorod Face Off: Comparing the heating efficiency, cellular internalisation and thermoablation capacity of gold nanorods and nanoprisms"

Gabriel Alfranca Ramón[1,2§], Álvaro Artiga [§], Grazyna Stepien[3], María Moros[4], Daxiang Cui[2], Scott G. Mitchell[1*] and Jesús M. de la Fuente[1,2,*]

1 –Instituto de Ciencia de Materiales de Aragón (ICMA-CSIC), Universidad de Zaragoza, 50009-Zaragoza, Spain;

2 – Institute of Nano Biomedicine and Engineering, Key Laboratory for Thin Film and Microfabrication Technology of the Ministry of Education, Shanghai Jiao Tong University, 200240-Shanghai, P. R. China;

3 – Instituto de Nanociencia de Aragón, Universidad de Zaragoza, 50018-Zaragoza, Spain;

4 - Istituto di Scienze Applicate e Sistemi Intelligenti "Eduardo Caianiello", 80078-Naples, Italy.

Authors for correspondence: *scott@unizar.es, *jmfuente@unizar.es

[§] these authors contributed equally to this publication

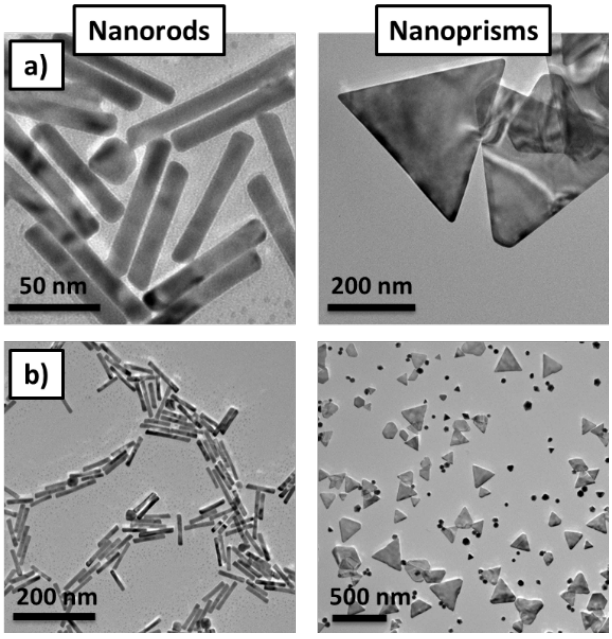

Figure S1 – Nanoparticle morphology. a) Transmission Electron Microscopy (TEM) and b) Scanning Electron Microscopy (SEM) of gold nanorods (NRs) and nanoprisms (NPrs).

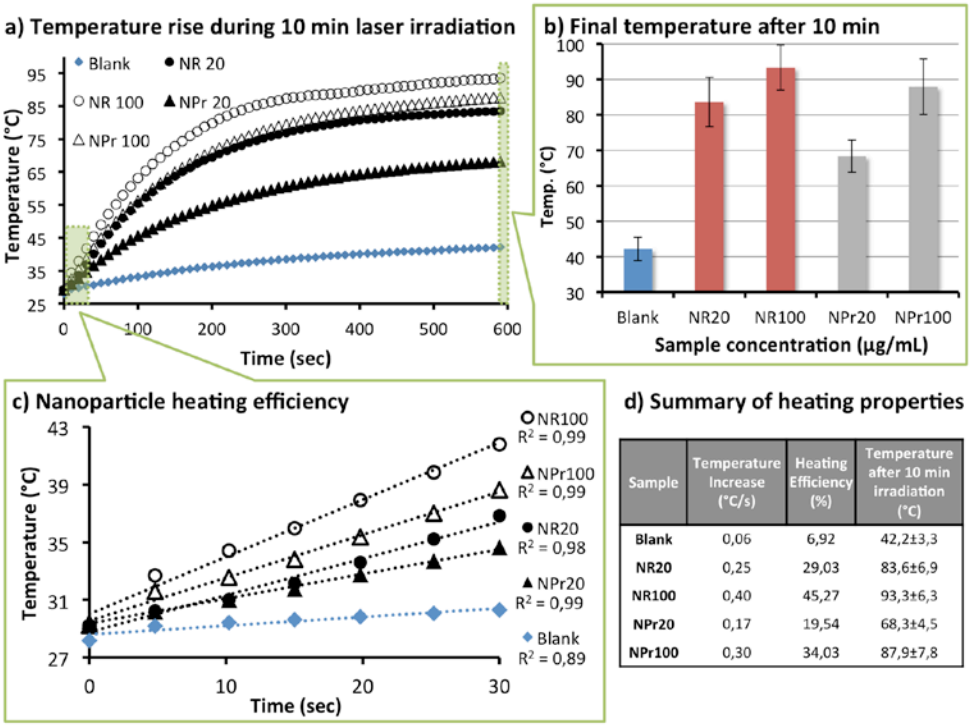

Sample	Temperature Increase (°C/s)	Heating Efficiency (%)	Temperature after 10 min irradiation (°C)
Blank	0,06	6,92	42,2±3,3
NR20	0,25	29,03	83,6±6,9
NR100	0,40	45,27	93,3±6,3
NPr20	0,17	19,54	68,3±4,5
NPr100	0,30	34,03	87,9±7,8

Figure S2 – Characterization of the heating capability of the nanoparticles. a) temperature rise of DMEM + different NN or NR concentrations during the 10 min laser irradiation period; b) the final temperature of the cell culture medium recorded after 10 min irradiation c) plot of the nanoparticle heating efficiency during the most linear rise in temperature (first 30 seconds); d) tabulated heating property data.

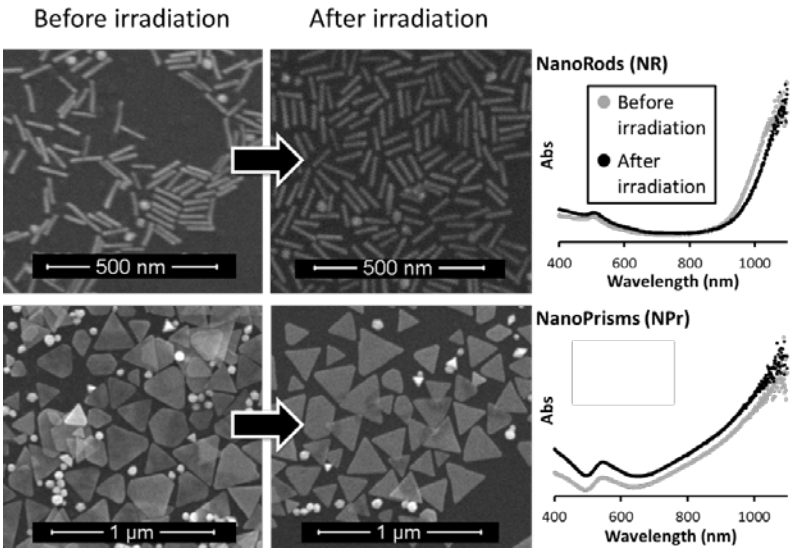

Figure S3 – Nanoparticle stability studies. SEM imaging and UV-Vis spectroscopy of the nanoparticles before and after irradiation of the laser for 10 min operating at 1.1 W. The conditions of irradiation affected neither the morphology nor the UV-vis spectra. The increase in the absorbance showed in the UV-Vis is caused by a decrease of the volume of the sample due to evaporation through the process.

SEM: Scanning Electron Microscopy.

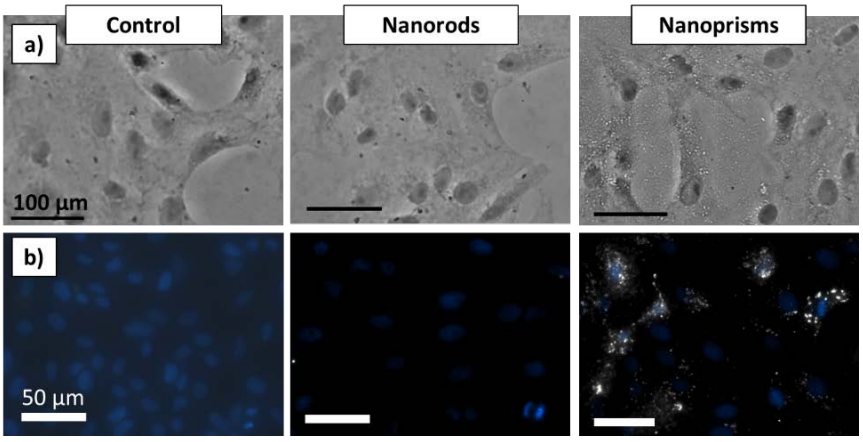

Figure S4 – Optical imaging of the cellular internalisation of AuNPs. (a) Bright-field phase contrast images and (b) Dark-field images showing the nucleus stained with DAPI (blue), where white contrast areas correspond to AuNPs. This figure illustrates how NPrs were homogeneously distributed inside the cytoplasm, were not attached to the cell membrane and did not form extended aggregated structures, while NRs were unable to be detected by dark field.